

UKAEA-CCFE-PR(21)11

L. Xiang, F. Militello, D. Moulton, F. Subba, L. Aho-  
Mantila, D. Coster, M. Wensing, T. Lunt, M.  
Wischmeier, H. Reimerdes

# **Understanding the effects of super-X divertor configuration on optimizing the operational space in DEMO**

Enquiries about copyright and reproduction should in the first instance be addressed to the UKAEA Publications Officer, Culham Science Centre, Building K1/O/83 Abingdon, Oxfordshire, OX14 3DB, UK. The United Kingdom Atomic Energy Authority is the copyright holder.

The contents of this document and all other UKAEA Preprints, Reports and Conference Papers are available to view online free at [scientific-publications.ukaea.uk/](https://scientific-publications.ukaea.uk/)

# **Understanding the effects of super-X divertor configuration on optimizing the operational space in DEMO**

L. Xiang, F. Militello, D. Moulton, F. Subba, L. Aho-Mantila, D. Coster, M. Wensing, T. Lunt, M. Wischmeier, H. Reimerdes



# The Operational Space for Divertor Power Exhaust in DEMO with a super-X Divertor

L. Xiang<sup>1\*</sup>, F. Militello<sup>1</sup>, D. Moulton<sup>1</sup>, F. Subba<sup>2</sup>, L. Aho-Mantila<sup>3</sup>, D. Coster<sup>4</sup>, M. Wensing<sup>5</sup>, T. Lunt<sup>4</sup>, M. Wischmeier<sup>4</sup>, H. Reimerdes<sup>5</sup>

<sup>1</sup>UKAEA-CCFE, Culham Science Centre, Abingdon, OX14 3DB, UK

<sup>2</sup>Politecnico di Torino, Corso Duca degli Abruzzi 24, 10129, Torino, Italy

<sup>3</sup>VTT, Technical Research Centre of Finland, FI-02044 VTT, Finland

<sup>4</sup>Max-Planck Institut für Plasmaphysik, D-85748 Garching, Germany

<sup>5</sup>Swiss Plasma Center (SPC-EPFL), CH-1015 Lausanne, Switzerland

E-mail: [lingyan.xiang@ukaea.uk](mailto:lingyan.xiang@ukaea.uk)

**Abstract.** SOLPS-ITER simulations of European DEMO reactor with a super-X divertor which has larger major radius at the outer target and increased connection length, show an increased operational space for divertor power exhaust compared to the conventional single-null configuration. Using a multi-fluid approach with fluid neutrals and charge state bundling of impurities, we assessed the existence and the boundaries of the operational space in the single-null and super-X configurations by carrying out fueling, seeding and power scans. Comparing to the conventional single-null divertor, super-X divertor is found to offer lower impurity concentration (factor  $\sim 2$  lower) at the same main plasma density, and consistently with this, it has lower main plasma density at the same impurity concentration level. This observed difference is in line with the simple analytical Lengyel model predictions resulting from the increased connection length in the super-X configuration. DEMO with a super-X divertor demonstrates remarkable robustness against increases in the input power, and in this study is able to exhaust the maximum expected steady-state separatrix-crossing power of 300 MW while maintain acceptable impurity concentration along the separatrix, something that was not possible in the single-null configuration in this study. This robustness of the super-X divertor lies mostly in its capability to sufficiently dissipate power in its divertor via argon radiation at acceptable argon concentration, which is related to two factors: long (with respect to single-null) parallel connection length from the upstream to the outer target and higher extrinsic impurity concentration at higher input powers. Finally, consistent with neon-seeded simulations of ITER, it is observed in all our simulations that the plasma density drops with increasing argon concentration given fixed power input. We find that as argon content increases, the accompanying enhancement of argon radiation reduces the power available for deuterium to get ionized, thus limiting the deuterium ionization particle source, and consequently reducing the plasma density.

## 1. Introduction:

The European fusion reactor DEMO is designed to produce 2 GW of fusion power [1]. Of this power, 20% goes to  $\alpha$ -particles that heat the plasma and needs ultimately to be handled in some ways. Additionally, the auxiliary heating schemes mainly for plasma control purposes will lend another 50 MW [2, 3] to the hot plasma. The total power to be exhausted thus tallies to 450 MW. In the current design, two thirds of this power is to be dissipated within the confined region of the plasma, of which about 150 MW is in the form of bremsstrahlung and synchrotron radiation by charged particles [4] and another 150 MW is via impurity line radiation. The power left to cross the separatrix into the plasma boundary region, denoted as  $P_{SOL}$ , is about 150 MW which is just above the L-H transition threshold. The average *unmitigated* power load to the divertor targets can be estimated, assuming no loss of power to the main chamber wall (mcw) by cross-field transport and homogeneous power spread on the targets, as

$$\begin{aligned} q_{\perp,t} &= q_{\parallel,t} * \sin\alpha \\ &= \frac{f_{odiv} * P_{SOL}}{2\pi R_u * \lambda_q * \sin\theta} \frac{1}{R_t/R_u} * \sin\alpha \end{aligned} \quad (1)$$

where  $f_{odiv}$  is the fraction of  $P_{SOL}$  that goes to the outer divertor,  $\alpha$  is the field line incident angle at the divertor target,  $\theta$  is the upstream magnetic field pitch angle, and  $R_t$ ,  $R_u$  are the major radius at the outer divertor target and the outboard midplane upstream. The 'u' and 't' in the subscript will be used to denote 'upstream' and 'target' throughout the paper.  $R_u = R_0 + a$ , with  $R_0$  being the major radius at the magnetic axis and  $a$  being the plasma minor radius.

Substituting the design parameters of DEMO conventional single-null divertor (SND) configuration [5], namely  $P_{SOL} = 150 \text{ MW}$ ,  $R_0 = 8.77 \text{ m}$ ,  $a = 3.1 \text{ m}$ ,  $\lambda_q = 3 \text{ mm}$ ,  $\theta = 20^\circ$ ,  $R_t/R_u = 0.75$ ,  $\alpha = 1.5^\circ$  and assuming  $f_{odiv} = 50\%$ , into equation (1), we have  $q_{\perp,t}^{SN} \approx 35 \text{ MWm}^{-2}$ . Note that  $\alpha = 1.5^\circ$  is a rather optimistic assumption here. The current engineering limit of stationary power load on tungsten divertor plate for sufficient duty cycle is about  $10 \text{ MWm}^{-2}$  [6]. Taking into consideration material degradation due to neutron irradiation, the power load due to photons and deuterium neutrals onto material surface, the tolerated plasma heat flux onto the divertor plates is about  $q_{\perp,t}^{limit} = 5 \text{ MWm}^{-2}$  [7, 8]. This limiting value is factor  $\sim 7$  lower than the estimated unmitigated power flux, which means that the excessive 86% of the power therefore needs to be radiated away mainly by extrinsic impurities in the thin plasma boundary region.

High impurity concentration in the vicinity of the main plasma threatens to compromise the fusion performance if the impurities get transported further inside the confined region. Some alternative divertor configuration designs guided by theory could be able to ease the burden of power exhaust in the plasma boundary region. In this work, efforts have been made to assess if the super-X divertor configuration harbors safe divertor operation without accumulating high impurity concentration near

the confined region. We will present the most recent results of the study on super-X divertor (SXD) [5] configuration for DEMO in the following. New results of other alternative configurations such as double-null and X-divertor are reported in [9, 10].

parameters	SXD	SND
$L_{\parallel,it}$	226m	191m
$L_{\parallel,ot}$	175m	100m
$L_{\parallel,it}/L_{\parallel,ot}$	1.30	1.91
$\alpha$	$\approx 1.5^\circ$	$\approx 1.5^\circ$
$f_x$	$\approx 1$	$\approx 0.75$

**Table 1.**  $L_{\parallel,it}$ ,  $L_{\parallel,ot}$  are the parallel connection lengths from the outboard midplane to the inner targets and outer target, respectively.  $\alpha$  is the field line incident angle at the target in the width of the power decay length  $\lambda_q$  on both sides of the strike point.  $f_x$  is the toroidal flux expansion at the outer target. Values are given here for the flux tube at  $\lambda_{dq}$  distance from the separatrix in the scrape-off-layer.

### 1.1. DEMO super-X divertor configuration

A poloidal cross-sectional view of the DEMO SXD configuration is given in figure 1. Due to the limit on TF coils stress and the requirement of remote handling, the outer target is set to a similar major radius as the outboard midplane (OMP), whose position is marked out in the figure. The toroidal flux expansion,  $f_x = R_t/R_{omp}$ , at the outer target with respect to the OMP is thus  $f_x \approx 1$ . Substituting the design parameters of DEMO SXD into equation (1), one sees that DEMO SXD, with factor  $\sim 1.33$  higher toroidal flux expansion than SND, has an *unmitigated* power flux to the target of  $q_{\perp,t}^{SX} \approx 26 MWm^{-2}$  at  $P_{SOL} = 150 MW$ . Now about 80% of  $P_{SOL}$  needs to be radiated in the plasma boundary and divertor volume. The longer connection length to the outer target in SXD further offers advantages over the conventional SND.

The SXD has longer parallel connection lengths from the OMP to the outer divertor target,  $L_{\parallel,ot}$ , than the conventional SND. The difference  $L_{\parallel,ot}^{SX}/L_{\parallel,ot}^{SN}$  is  $\geq 1.75$  in the radial range of the power decay length of  $\lambda_q = 3 mm$ , see table 1. The 2-point model predicts  $T_u^{7/2} - T_t^{7/2} = \frac{7}{2} \frac{q_{\parallel,u}}{\kappa_{e0,\parallel}} * L_{\parallel}$  [11]. Therefore, longer connection length means lower divertor target temperature, given comparable upstream plasma conditions. Furthermore the parallel connection lengths from the OMP to the inner and outer divertor targets,  $L_{\parallel,it}$ ,  $L_{\parallel,ot}$ , are rather comparable in DEMO SXD. Their ratio  $L_{\parallel,it}/L_{\parallel,ot}$  is in the range of 1.08 – 1.3 in the radial range of  $\lambda_q$ , compared to 1.3 – 1.95 in DEMO SND. According to the 2-point model, this may contribute to better symmetry between the inner and outer divertor in SXD[12], as the model predicts that  $q_{\parallel,odiv}/q_{\parallel,idiv} \propto L_{\parallel,it}/L_{\parallel,ot}$ , where 'odiv' and 'idiv' stand for outer divertor and inner divertor. At the radial location of  $\lambda_q = 3 mm$ , the connection length to the inner and outer divertor targets are given in table 1. The values of SND are also provided as reference.

## Operational Space in DEMO with a super-X Divertor

4

### 1.2. Simulation database

More realistic estimation of the targets power load in DEMO SXD needs to be done through modeling with models more complete than the 0D 2-point model. The code package SOLPS-ITER [13, 14], which consists mainly of 2D fluid plasma code B2.5 [15] and 3D kinetic neutral code Eirene [16, 17], is implemented with vigorous boundary plasma physics models. The aim of this study is to assess the accessibility of the *operational space* of DEMO SXD and how it compares to that of the DEMO SND configuration. The constraints used to define the operational space for DEMO reflect the considerations of ensuring sufficient lifetime of the divertor targets and simultaneously

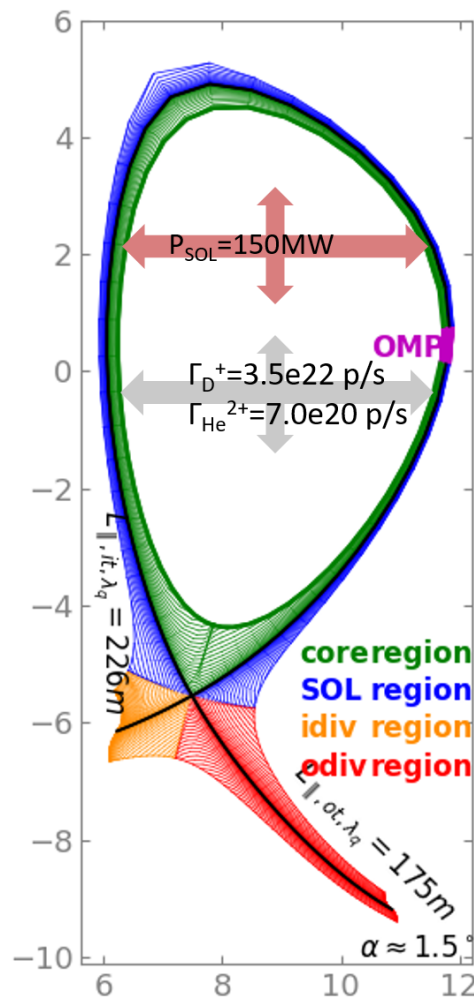


**Figure 1.** Poloidal cross-section of DEMO SXD configuration used in SOLPS-ITER simulation. The coloured regions form the modelling domain, and they are: the 'core' (green color), the SOL (blue color), the inner divertor (orange color), denoted as *idiv*, and the outer divertor (red color), denoted as *odiv* henceforth in figures. This notation of regions will be used in the following sections discussing about the modelling results. The location of the outboard midplane (OMP) is marked in magenta.  $L_{\parallel, it}$ ,  $L_{\parallel, ot}$  are the parallel connection lengths from the OMP to inner and outer targets.  $\alpha$  is the field line incident angle at the target around the strike point.

safeguarding fusion performance in the confined region.

We use the SOLPS-ITER code with fluid neutrals and argon charge state bundling in order to shorten the computational time to accommodate large parameters scans. In dense and cold divertor plasma conditions, the plasma and neutral densities are expected to be high and fluid neutral temperature (same as ions') is low. The mean free path of neutrals is short with respect to the DEMO divertor size. The SX divertor has width  $\geq 50$  cm and length  $\approx 5$  m, and the SN divertor's width is  $\geq 1$  m and length is  $\approx 2$  m, see figure 1&2 in [5]. Aftermath estimation of the neutrals' ( $D0$  and  $Ar0$ ) mean free path in the simulations with cold divertor condition ( $T_{e,target} \leq 5$  eV) is in the order of cm. Therefore, the fluid neutrals approach is considered appropriate here. We consider a deuterium (D) plasma, with intrinsic impurity helium (He) and extrinsic impurity argon (Ar). Ar is bundled into effectively 3 charge states:  $Ar^0$ ,  $Ar^{1+-17+}$ ,  $Ar^{18+}$ . The rate coefficients of the effective charge state  $Ar^{1+-17+}$  are computed from the ADAS rate coefficients of unbundled Ar using a charge state weighing algorithm introduced in the new ADAS416 manual [18]. Owing to the method of charge state bundling, any enhancement of the electron cooling coefficient function due to impurity transport is not accounted for [19]. All the neutral atoms are considered as fluids, as are all the charged species. The particle diffusivity is  $D_{\perp} = 0.1$  m<sup>2</sup>/s. The thermal conductivity of electrons and ions is  $K_{\perp,e,i} = 0.1$  m<sup>2</sup>s<sup>-1</sup> from  $-10$  mm to  $-2.5$  mm inside the separatrix, increases to  $0.3$  m<sup>2</sup>s<sup>-1</sup> at the separatrix, and remains  $0.3$  m<sup>2</sup>s<sup>-1</sup> in the SOL. Both  $D_{\perp}$  and  $K_{\perp,e,i}$  are down-scaled from the values used in ITER SOLPS-ITER simulations to obtain a power decay length at the outboard midplane of  $\lambda_q = 3$  mm. To assess the operational space, we varied both the D fuelling and Ar seeding rates, thus scanning an array of combinations of these two parameters. The ranges covered in the scan are:  $\Gamma_{D^0} = 2.55e22 \rightarrow 2.55e24$ , and  $\Gamma_{Ar^0} = 3.5e19 \rightarrow 3.5e21$ , with the unit [*particles/s*] (*[p/s]*). During the scan we obtained both attached and detached divertor conditions, here defined simply as electron temperature along the target being above or below 5 eV everywhere. We did the scan in the same manner for the SND, which covered very similar ranges of fuelling and seeding as the SXD. At the core boundary, i.e. the inner most green contour in figure 1, we imposed a deuterium ion flux of  $\Gamma_{D^+} = 3.5e22$  p/s to account for pellet fuelling, a helium ion flux of  $\Gamma_{He^{2+}} = 7.0e20$  p/s to be the He produced during the fusion reaction, and input power  $P_{in\ddagger}$  of 150 MW split evenly into electron and ion channels entering the simulation domain. To test the robustness of DEMO SX divertor against  $P_{SOL}$  fluctuations, we also performed simulations at an increased power input of 300 MW, assuming the extreme case where no line radiation happens in the core region.

$\ddagger$   $P_{in}$  is similar to the aforementioned  $P_{SOL}$  in the context of SOLPS-ITER modelling. Strictly speaking, they are not the same, as  $P_{in}$  refers the power into the simulation domain at the core boundary. But since the part of the simulation domain inside the separatrix is thin comparing to the entire confine region, as seen in figure 1.  $P_{in}$  and  $P_{SOL}$  are *effectively* equivalent, and mostly  $P_{in}$  will be used when talking about SOLPS-ITER simulations.

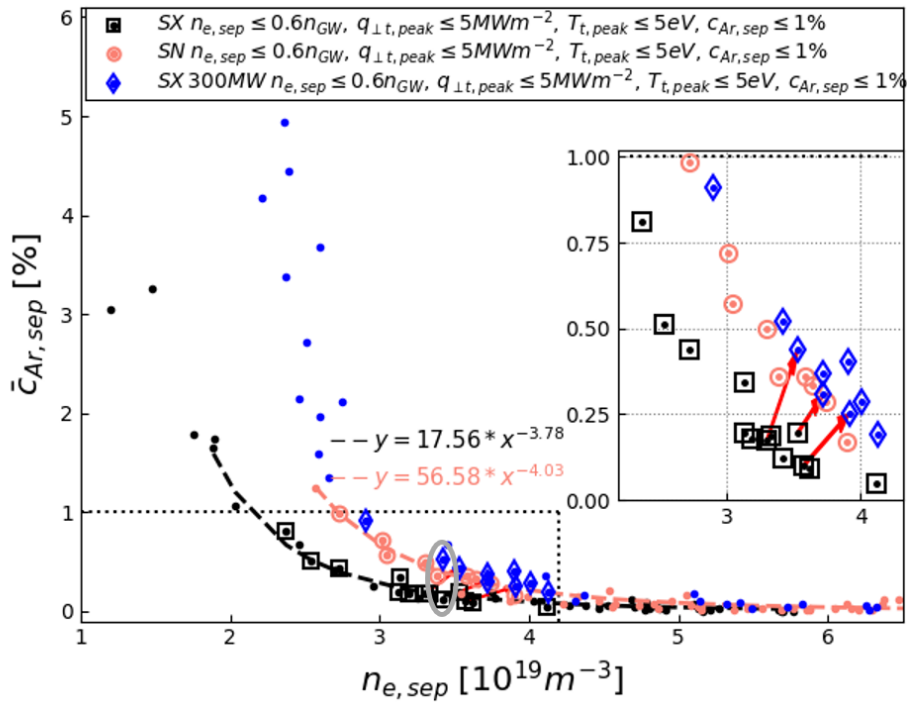


**Figure 2.** The average argon concentration along the separatrix  $\bar{c}_{Ar,sep}$  plotted against the density at the outboard midplane separatrix  $n_{e,sep}$  for all the simulations done for a configuration (SX (black) or SN (pink)), or an input power level ( $P_{in}=150\text{MW}$  or  $300\text{MW}$  (blue)). Among them, the simulations whose the plasma is within the operation space are additionally marked with symbols (square, circle, diamond). The black and pink dash lines are the power law fit to the data points of SX and SN. An insert showing only the points within the operation space is also given. The three red arrows connect three pairs of simulations of SXD with the same fuelling and seeding rates but at different  $P_{in}$ .

## 2. Operational space for DEMO divertor

A DEMO plasma must satisfy *at the least* the following three requirements concerning the plasma side to be considered as operationally viable: (1) no disruptions or H-L back transition due to too high plasma density, (2) long enough lifetime of the divertor plasma facing components (PFCs), and (3) low impurity level in the main plasma to safeguard sufficiently high rate of fusion reaction in the core. These requirements are quantified as constraints imposed on certain plasma parameters in this work to easily assess if a simulated DEMO plasma satisfies them. The constraints are the following:

- The stationary peak plasma power flux at all targets is below the limit for tungsten, i.e.  $q_{\perp,t} \leq 5 \text{ MWm}^{-2}$ .
- The target temperature is sufficiently low to avoid significant tungsten net erosion. We set the limit to be  $T_t \leq 5\text{eV}$ .
- The density at the separatrix,  $n_{e,sep}$ , does not exceeds some fraction of the Greenwald density limit  $n_{GW}$  to sail safe below the density limit disruption and

avoid H-L back transition at high densities. For DEMO  $n_{GW} = 7 \times 10^{19} m^{-3}$ . We put a constraint of  $n_{e,sep} \leq 0.6n_{GW} \approx 4.2 \times 10^{19} m^{-3}$ .

- The extrinsic impurity concentration at the immediate vicinity of the confined region should not be too high to spoil the fusion performance. SOLPS-ITER may not model the impurity transport in the confined region well. We nevertheless limit the argon concentration at the separatrix to be  $c_{Ar,sep} \leq 1\%$ , but trust more the comparison between configurations and power levels.

A modelled plasma which meets simultaneously these constraints is considered to be within the *operational space*.

### 2.1. Operational space in DEMO SXD and SND

Applying these constraints to the simulations with fuelling and seeding rates scan, we identify whether an operational space exists for a given divertor configuration and power level, and if this is the case, what are the differences in parameters of interest between the different configurations and input powers inside the operational space.

An operational space *could* be found for both the SND and the SXD when we impose 150 MW crossing the core boundary. But only the SXD has operational space at  $P_{in} = 300$  MW, while *no* acceptable solution could be found for the SND at this input power. In section 1, it is shown that in DEMO SND with  $P_{in} = 150$  MW the plasma boundary region needs to dissipate about 86% of  $P_{SOL}$  to reduce the target power flux from the *unmitigated* value of  $35$  MW/m<sup>2</sup> to the safe value of  $5$  MW/m<sup>2</sup>. Present day tokamaks have reported main plasma radiation fraction of 50%-70%, and the radiation fraction in the plasma boundary to be even lower [20, 21, 22, 23]. The existence of the operational space for SXD and particularly SND with  $P_{in} = 150$  MW is thus encouraging. The plasma conditions at the separatrix concern both the core performance and the divertor conditions. A good way to display our results is to plot the separatrix argon concentration as a function of the separatrix density, the former representing the amount of impurities needed to dissipate the plasma power and the amount of dilution, and the latter measuring core performance (lower density leads to improved pedestals). We plot these quantities for our database in figure 2.

Shown in this figure is the Ar concentration averaged along the separatrix above the X-point,  $\bar{c}_{Ar,sep}$ , and the density at the OMP,  $n_{e,sep}$  for all simulations of DEMO SND with  $P_{in} = 150$  MW and DEMO SXD with  $P_{in}$  being 150 MW and 300 MW. The SND with  $P_{in} = 300$  MW does not have an operational space found in the simulations, hence its data point not shown in this figure. One can see that the data points of a configuration or an input power level collapse onto a distinctive curve. The curves reveal that:

- (i) At the same density (*Ar concentration*), DEMO SXD has lower Ar concentration (*density*) than the SND. The insert in the figure, showing the operational points only, demonstrates that the difference is nearly a factor of 2. Furthermore, within the operational space SXD reaches lower density than SND does. These imply that

the DEMO SXD provides a larger margin in terms of lowest possible separatrix density or main plasma dilution.

- (ii) At  $P_{in} = 300$  MW SXD needs double the Ar concentration with respect to the SXD at  $P_{in} = 150$  MW at the same density. Note also that the SND curve nearly overlaps with that of the SXD at  $P_{in} = 300$  MW, despite a factor of 2 difference in their input power. This indicates that the SND has already exhausted its capability to radiate the power at  $P_{in} = 150$  MW, while the SXD still has some margin.
- (iii) For a plasma within the operational space in SXD configuration with  $P_{in} = 150$  MW, raising the power input to 300 MW the plasma *may* remain inside the operational space in some cases, as indicated by the red arrows in the insert in figure 2. On the contrary, we didn't find an operational space for DEMO SND at  $P_{in} = 300$  MW. This suggests that the SXD configuration is more robust in exhausting the power into the plasma boundary than the conventional SND.
- (iv) As Ar concentration increases along the curves, the plasma density decreases in all cases, regardless of divertor configuration or power level. The curves representing different configurations or  $P_{in}$  converge at higher  $n_{e,sep}$ . This is simply because the impurity concentration progressively becomes negligible towards higher densities, hence the effect of argon impurities on the plasma diminishes.

We will examine item (iii) and (iv) in section 3 and section 4 respectively, and elaborate on (i) and (ii) in the following.

The factor  $\sim 2$  difference in  $\bar{c}_{Ar,sep}$  at the same density in SXD and SND coincides with the difference in their parallel connection length from the OMP to the outer target, which is  $L_{||,ot}^{SX}/L_{||,ot}^{SN} \geq 1.75$  within distance of  $\lambda_q$  from the separatrix. A factor of 2 difference in  $\bar{c}_{Ar,sep}$  is also observed as the input power in the SXD is doubled: from 150 MW to 300 MW. As explained in section 1.1, longer connection length is beneficial in two ways: (1) when  $T_{eu}$  is comparable, longer connection length means lower temperature at the target; (2) when  $T_{et}$  is similar, configuration with longer connection length has higher upstream temperature. In figure 3(a), electron temperature  $T_e$  at the OMP separatrix is given at different densities for SXD and SND simulations. The simulations within the operational space all satisfy  $T_{t,peak} \leq 5$  eV, thus have similar temperatures at the target. We see that indeed the SXD simulations have higher upstream temperature than the SND. We will show that having a higher temperature upstream and similar temperature at the target means stronger radiative power dissipation in the divertor volume.

Lengyel model [24] estimates the impurity concentration  $c_z$  needed for detachment onset in the plasma boundary layer. It assumes (1) pure electron heat conduction in the parallel direction, (2) no radial transport, (3) power loss due entirely to impurity radiation, (4) homogeneous impurity concentration in the boundary layer, (5) conservation of static pressure within the impurity cooling region. With these

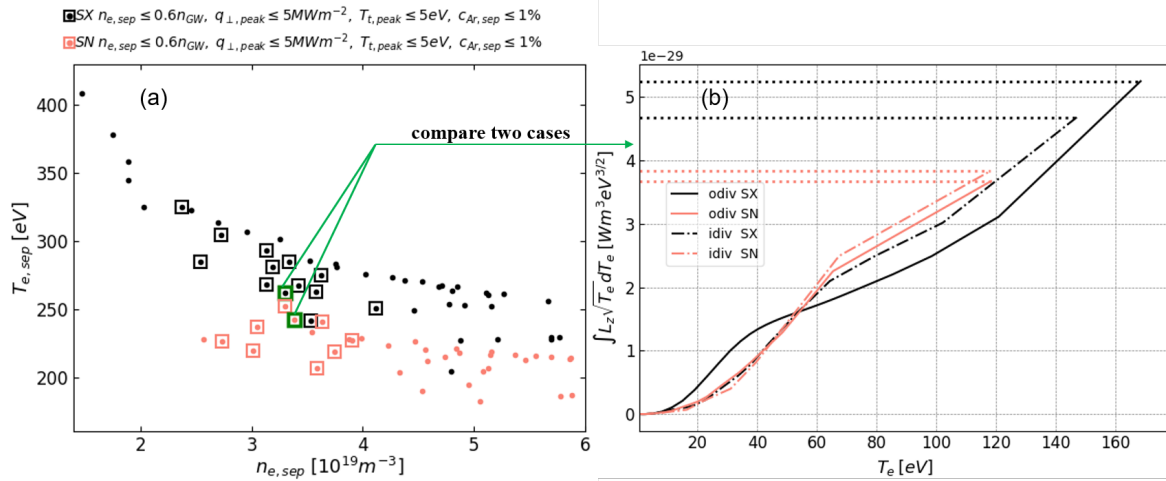


**Figure 3.** (a) *dots*: the upstream separatrix temperature as a function of the upstream separatrix density in each of the simulations of the SXD and SND configurations. The simulations within the operational space are marked additionally with square symbols. (b): Comparison of the Lengyel integral [24] as a function of the temperature in the inner and outer divertor for the two simulations marked in green square in (a). The two simulations are with similar upstream density and radiated power from the 'core' region.

assumptions, the  $c_z$  needed for detachment onset is given by:

$$c_z = \frac{q_{\parallel u}^2 - q_{\parallel t}^2}{2\kappa_{e0,\parallel} n_{eu}^2 T_{eu}^2 \int_t^u L_z(T_e) \sqrt{T_e} dT_e} \quad (2)$$

Here,  $\kappa_{e0,\parallel}$  is the parallel electron heat conductivity divided by  $T_e^{5/2}$ .  $L_z$  is the electron cooling coefficient of impurity ' $z$ '. The integral  $\int_t^u L_z(T_e) \sqrt{T_e} dT_e$  is henceforth referred to as the *Lengyel integral* and denoted as  $L_{int}$ .  $L_{int}$  represents the temperature dependent part of the radiated power by an impurity. We select two simulations, marked with green squares in figure 3(a), of SXD and SND with similar upstream density and radiation from the 'core' region. We compare the  $L_{int}$  in the inner and outer divertor volume as a function of  $T_e$  for the two simulations in figure 3b. Note that the  $L_{int}$  and  $T_e$  shown here are averaged values. We first calculate the radial average of  $T_e$  weighted by the density  $n_e$ , and the radial average of  $L_z$  weighted by the temperature in the cells at each poloidal location. With the radial average of  $T_e$ ,  $L_z$  and  $\sqrt{T_e}$ , we can calculate the average  $L_{int}$  within  $\lambda_q$  distance from the separatrix in the inner and outer divertor. One sees that in the SXD the Lengyel integral reaches higher values in the divertors than in the SND configuration, meaning the former could dissipate more power via radiation in the divertor volume.

As investigated in [25], as well as shown in figure 3(b),  $L_{int}$  has nearly *linear* dependence on  $T_{eu}$  for argon impurity,  $L_{int} \propto T_e$ . In detached conditions, the power flux downstream at the target,  $q_{\parallel t}$ , is negligible compared to the upstream power flux  $q_{\parallel u}$ .

Operational Space in DEMO with a super-X Divertor 10

Therefore the  $c_z$  in equation (2) can be rewritten as:

$$c_z \propto q_{\parallel u}^2 / (2\kappa_{e0,\parallel} n_{eu}^2 T_{eu}^3) \quad (3)$$

Substituting the 2-point model formula of  $T_{eu} \approx (\frac{2}{7} \frac{q_{\parallel u} L_{\parallel}}{\kappa_{e0,\parallel}})^{2/7}$  into equation (3) we obtain:

$$c_z \propto \frac{q_{\parallel u}^{1.14}}{n_{eu}^2 L_{\parallel}^{0.86}}. \quad (4)$$

Now the observed difference in argon concentration between SXD and SND and between SXD with  $P_{in}=150$  MW and  $P_{in}=300$  MW can well be explained by the analytical Lengyel model. The trends discussed in item (i) and (ii) above are well captured by equation (4). This equation reveals that, on one hand, at the same density and the same power flux upstream, the argon concentration needed for divertor detachment onset is *inversely proportional* to the connection length from the midplane to the outer target. Being inside the operational space requires a cold divertor plasma condition of  $q_{\perp,t} \leq 5MWm^{-2}$  and  $T_t \leq 5eV$ . We checked that the simulations within the operational space are at/after the target ion flux 'roll-over'. For DEMO SND and SXD, having the same  $\lambda_q$ , their upstream power flux is similar at the same input power of  $P_{in}=150$  MW. The parallel connection length at radial distance of  $\lambda_q$  is  $L_{\parallel}^{SX} / L_{\parallel}^{SN} = 175m / 100m = 1.75$ . The Lengyel model thus predicts that the averaged argon concentration at detachment onset in the plasma boundary is  $\bar{c}_{Ar}^{SX} / \bar{c}_{Ar}^{SN} \approx 0.57$ , which explains point (i) observed in figure 2. On the other hand, according to this equation 4, at the same upstream density the argon concentration needed at the divertor detachment onset is *proportional* to the upstream parallel power flux which in the same configuration is effectively the input power. Hence for SXD at  $P_{in} = 150$  MW and 300 MW, with the input power doubled, the  $\bar{c}_{Ar,sep}$  needed is predicted to double as well. Therefore, what we stated above in point (ii), comparing the 300 MW and the 150 MW simulations for, is explained by equation 4.

In addition to the advantage outlined in point (i), the DEMO SXD configuration has more advantageous radiation pattern than the SND. Illustrated in figure 4 is the radiated power in the outer divertor against the radiation above the X-point, both as a fraction of the input power. Shown here are only simulations within the operational space. We see that, consistent with the lower level of argon impurity concentration along the separatrix, the radiation from the main plasma region ('core'+SOL) in the SXD is always lower than that in the SND at the same input power of  $P_{in}=150$  MW. The radiated power fraction above the X-point is between 7% to 16% in SXD and between 19% to 36% in SND. This suggests that the DEMO SXD configuration needs *less* radiation from the main plasma region to be within operational parameters space. At the same time, the radiated power inside the *outer* divertor for the simulations within the operational space is significantly higher in SXD than in SND, the largest difference being around factor  $\sim 2$ . However, the advantage is less marked for the inner divertor leg where the two configurations exhibit more comparable radiation capability. The figure

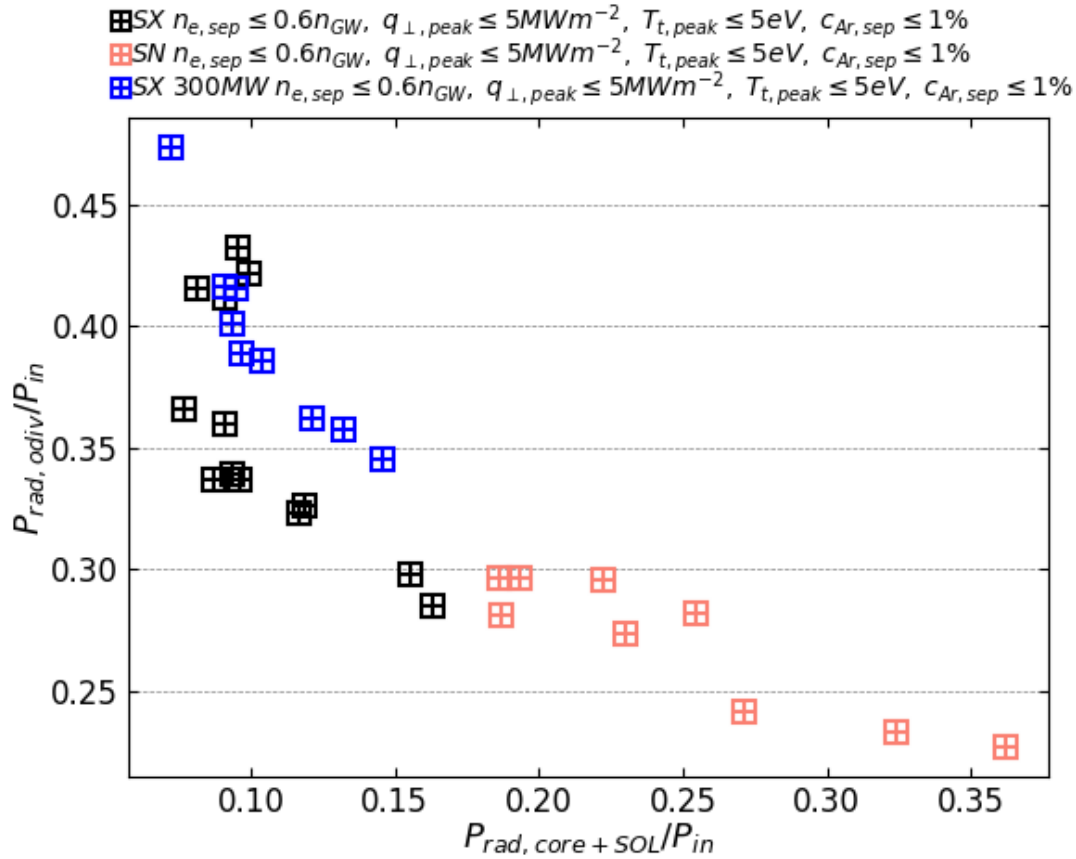


**Figure 4.** The radiated power in the outer divertor as a function of the fractional radiated power from the 'core' and SOL region (see definition in figure 1) above the X-point, both as fraction of the input power  $P_{in}$ . Only the simulations within the operational space are shown here for DEMO SXD at  $P_{in}=150$  MW and  $P_{in}=300$  MW, and SND at  $P_{in}=150$  MW.

also illustrates that when the input power is doubled, the radiation fraction in the *outer* divertor can be higher at the same main plasma radiation fraction. Namely, the *outer* divertor leg of the SXD configuration can radiate even more efficiently at higher input power, keeping the radiation in the main plasma region low.

This is confirmed also in figure 5 where the 2D radiation distributions for three simulations are shown. These three simulations, outlined by the grey ellipse in figure 2, have similar upstream density. Here, we see straightforwardly that the radiation above the main plasma region is the lowest in the SXD with  $P_{in}=150$  MW, and is the highest in the SND at  $P_{in}=150$  MW. Notice that, the absolute radiated power from above the X-point in SXD with  $P_{in}=300$  MW is still slightly lower than that in SND with  $P_{in}=150$  MW, despite the doubled input power. Apart from this, figure 5 also reveals two things about the radiation pattern in the divertor region: First, the divertor radiation is largely confined close to the targets in SXD at  $P_{in}=150$  MW, whereas in SND it extends along the length of the divertor leg to the X-point. Second, when the input power is doubled to 300 MW in SXD, the radiation in the inner and outer divertor legs both extend towards

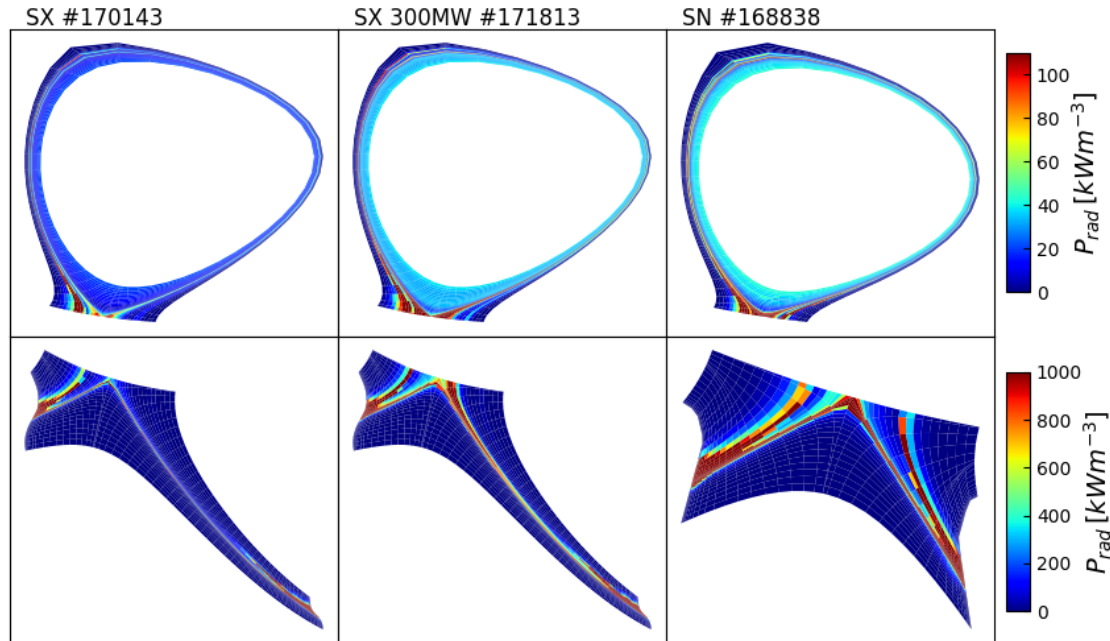


**Figure 5.** The total radiated power density distribution in the modelling domain for 3 selected simulations outline by the grey ellipse in figure 2, which are simulations within the operational space with similar upstream density. The upper row shows the radiation density distribution in the regions above the X-point, i.e. in the 'core' and SOL. The lower row shows the radiation density distribution in the divertor region.

the X-point, resembling now the patterns in SND. Besides the extension upward along the poloidal direction, the strong radiation band in the outer divertor also expands in the radial direction at  $P_{in}=300$  MW, comparing to SXD at  $P_{in}=300$  MW.

### 3. Understanding the robustness of the SXD

As pointed out in item (iii) in section 2.1, when the input power is doubled from 150 MW to 300 MW while the fuelling and seeding rates are kept the same in SXD simulations, e.g. the 3 pairs of simulations indicated by the red arrows in figure 2, the plasma adjusts itself to higher density and Ar concentration levels, and dissipates the extra power. In order to identify what changed in the plasma that ultimately enabled it to exhaust double the amount of power and to stay within the operational space the SXD configuration, we look at one of these pairs of simulations in detail.

With  $P_{in}$  increased from 150 MW to 300 MW at the same fuelling and seeding rate, the upstream plasma evolves to be slightly denser as indicated in figure 2, as well as much hotter. The radial profiles at the OMP in figure 6 shows that the density is factor  $\sim 1.09$  higher (*by 9%*), and temperature is factor 1.43 higher (*by 43%*) in the radial

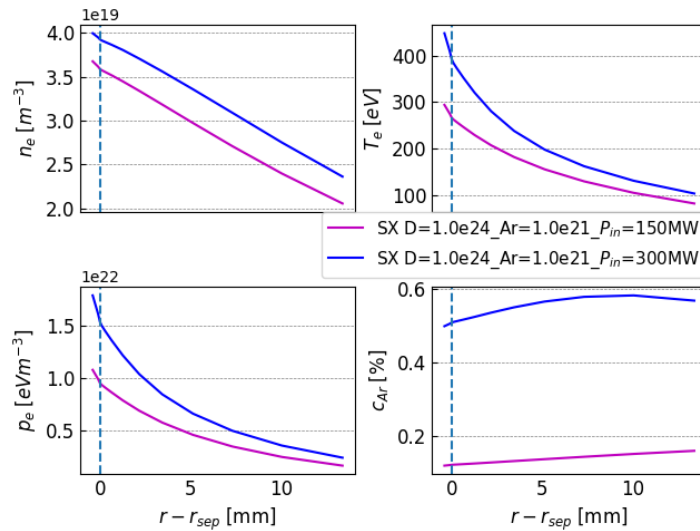


**Figure 6.** The radial profiles of electron density, temperature, static pressure and argon concentration at the outboard midplane in two DEMO SXD simulations with same deuterium fuelling and argon seeding rates at  $P_{in}=150$  MW and  $P_{in}=300$  MW.

width of  $\lambda_q = 3$  mm from the separatrix. The electron static pressure in the denser and hotter plasma is hence about factor  $\sim 1.5$  higher. We also notice that the local (OMP) Ar concentration is higher across the width of SOL at higher power input. Between the SXD and the SND, as discussed in section 2.1, at the same density (*concentration*) the former has *lower* concentration (*density*). This is an essential advantage of SXD, as here we observe that the plasma shifts to higher density and higher concentration when the power input is doubled. The direct reason why DEMO SND does not have operational space at  $P_{in} = 300$  MW may be that it needs too high density ( $n_{e,sep} > 0.6n_{GW}$ ) and too high Ar concentration ( $c_{Ar,sep} > 1\%$ ) to achieve safe divertor conditions ( $q_{\perp,t} \leq 5$  MWm $^{-2}$  and  $T_t \leq 5$  eV), as the density and concentration are already high at  $P_{in} = 300$  MW.

Indeed argon concentration increases everywhere in the simulation domain at higher input power in SXD, as demonstrated by figure 7(b). The concentrations shown here are the average value in each region weighted by the cell volume. Outside the separatrix, the average is done over grid cells within the width of  $\lambda_q$  from the separatrix. One sees that the average Ar concentration is about  $\times 1.6$  higher in the outer divertor, and about  $\times 1.5$  higher in the inner divertor. Its level increases particularly in the main plasma ('core'+SOL) but the absolute values remain low, and as we will see in figure 7(a), the radiated power in the these two regions stays low as well. The radiated power, decomposed by species (D or Ar) and by region, is shown here in figure 7(a). Corresponding to the increase of averaged Ar concentration in each region  $\bar{c}_{Ar,\#}$ , the radiation increases everywhere in the case of  $P_{in}=300$  MW. In both the 150 MW and the 300 MW simulations, the radiation is concentrated in the divertor region. The radiation is enhanced particularly in the divertor region, with the absolute radiated power being about a factor of  $\sim 2.3$  higher in the  $P_{in}=300$  MW simulation in both the inner and outer divertor leg. Figure 7(a) also reveals that the enhancement of the radiation at  $P_{in}=300$

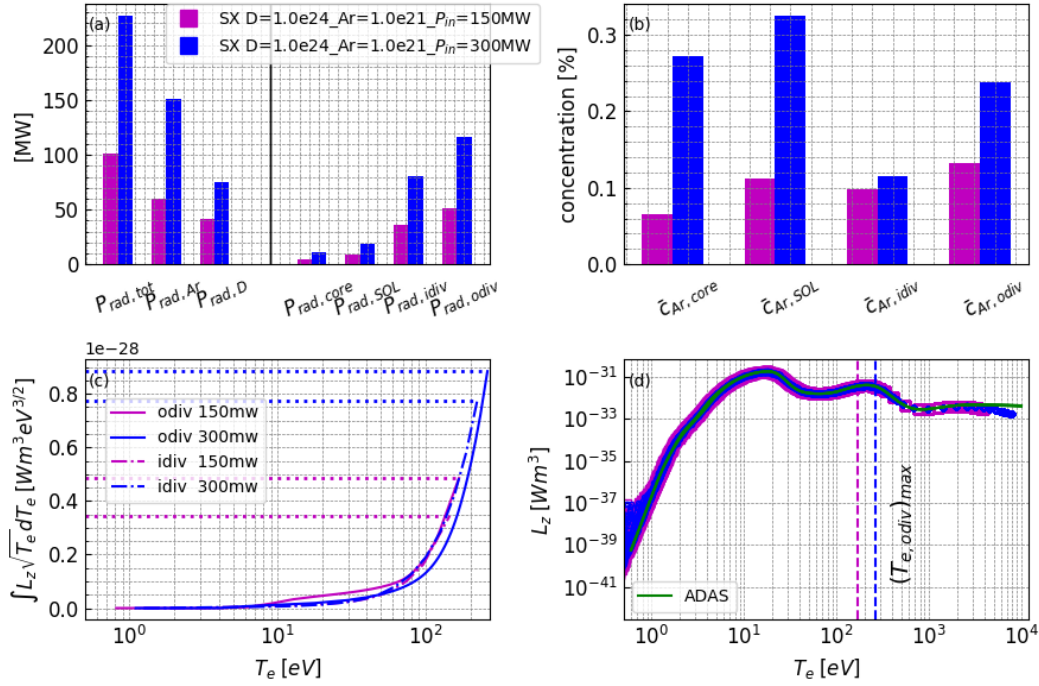


**Figure 7.** Comparison of various parameters of the plasma for two DEMO SXD simulations with same deuterium fuelling and argon seeding rates at  $P_{in}=150$  MW and  $P_{in}=300$  MW. (a) The radiated power fractions  $f_{rad,\#}$  with respect to  $P_{in}$ , with ‘#’ denoting radiation of a species from the entire modelling domain or radiation in a region from all the species. (b) The averaged argon concentration in each region. (c) The average *Lengyel integral* (equation 2) as a function of  $T_e$  in the flux tubes within  $\lambda_q$  distance from the separatrix in the inner and outer divertor. (d) The the electron cooling coefficient calculated from the modelling results and from ADAS database. The vertical dashed lines marked the radial average of the temperature at the divertor entrance at the poloidal location of the X-point, which is also the upper bound of the temperature over which the Lengyel integral is calculated.

MW is contributed predominantly by the Ar impurity. The Ar radiation in the domain increases *by* 150%, leading the total radiation to increase *by* 130%, more than the 100% increase of the input power  $P_{in}$ . Because of the more than doubled enhancement of impurity radiation in the divertor region in the SXD configuration, the plasma is able to stay within the operational space when the input power is increased from 150 MW to 300 MW.

To understand *why* argon radiation can greatly increase in the divertor region in the higher power plasma, we return to the Lengyel model shown in equation 2. Given that for plasma within the operational space  $q_{\parallel,t} \ll q_{\parallel,u}$ , we reform the equation as:

$$q_{\parallel u} \approx \sqrt{2\kappa_{e0,\parallel} c_z (n_{eu} T_{eu})^2 \int_t^u L_z \sqrt{T_e} dT_e} = \sqrt{2\kappa_{e0,\parallel} c_z (n_{eu} T_{eu})^2 L_{int}} \quad (5)$$

Multiplying by the contact surface area, the r.h.s yields the total power loss due to impurity radiation (Lengyel model assumption (3)) in the region between the upstream

and the target. The three terms that regulate the radiated power in this equation are:  $c_z$ ,  $n_{eu}T_{eu}$  and the *Lengyel integral*  $L_{int}$ . As pointed out above, due mainly to the increase of  $T_{eu}$  at  $P_{in}=300$  MW the electron static pressure  $p_{eu} = n_{eu}T_{eu}$  is about factor  $\sim 1.5$  higher, and the average Ar concentration within the distance of  $\lambda_q$  from the separatrix in the divertor region  $\bar{c}_{Ar,odiv}$  and  $\bar{c}_{Ar,div}$  are  $\times 1.65$  and  $\times 1.5$  higher respectively at  $P_{in}=300$  MW, compared to the SXD with  $P_{in}=150$  MW. The remaining term is  $L_{int}$  which depends on the electron temperature  $T_e$ . Because the electron cooling coefficient  $L_z$  drops by several orders at temperatures below 5 eV, the integration is not sensitive to the exact value of  $T_t$  as long as it is  $\leq 5$  eV. Therefore for simulations within the operational space, the Lengyel integral depends only on  $T_u$ . Electron temperature increases from the target to upstream along each single flux tube. We calculate the average  $L_{int}$  within  $\lambda_q$  distance from the separatrix in the inner and outer divertor in the same way as explained in section 2.1. We display the calculated  $L_{int}$  as a function of the temperature in figure 7(c). The position of the upper limit of the temperature for the integration is marked out in figure 7(d), which also shows the Ar electron cooling function from ADAS and that obtained from the simulation. In this figure we see again that  $L_{int}$  increases nearly linearly with the upper bound of the temperature for argon impurity. Because the temperature at the divertor entrance is higher in the  $P_{in}=300$  MW case, the  $L_{int}$  in the inner and outer divertor leg reach larger values. The integral is factor  $\sim 1.8$  higher in the outer divertor and factor  $\sim 2.2$  higher in the inner divertor, compared to the standard  $P_{in}=150$  MW case. Inserting the factors of differences in  $n_{eu}T_{eu}$ ,  $c_z$  and the  $L_{int}$  into the r.h.s. of equation 5, we have that  $\left(\sqrt{c_z(n_{eu}T_{eu})^2 L_{int}}\right)_{300MW} / \left(\sqrt{c_z(n_{eu}T_{eu})^2 L_{int}}\right)_{150MW} \approx 2.5.$ , in both the outer and inner divertor. This is close to the observed 135% increase of Ar radiation in the divertors and 150% increase in domain. Therefore, the combined result of elevated upstream electron pressure, Ar concentration, and larger values of *Lengyel integral* enables the plasma to exhaust the extra power in the divertor region, when the input power is doubled in the SXD configuration while the fuelling and seeding rates remain the same. We stress that the increase of electron pressure and the Lengyel integral is due to an increase of the upstream electron temperature. This is plain to see when we examine two SXD simulations at similar upstream density with  $P_{in}=150$  MW and  $P_{in}=300$  MW, both within the operational space. The Ar radiation in the outer divertor of two such cases are different by about a factor of  $\sim 2.4$ . The temperature alone being factor  $\sim 1.6$  higher in the 300 MW case, leading the electron pressure and the Lengyel integral to be factor  $\sim 1.6$  and factor  $\sim 1.8$  higher. Combining with the change in the Ar concentration level, we reproduce in equation 5 the factor of change of Ar radiation in the divertors.

#### 4. Impurity seeding affecting upstream plasma density

Finally, we look into point (iv) raised in section 2.1. Here we will explain the observed plasma density drop with increasing Ar concentration. As this is observed for different configurations and input powers examined in this work, we focus on the DEMO SXD

## Operational Space in DEMO with a super-X Divertor

16

at standard  $P_{in}=150$  MW.

Similar reduction of the main plasma density is observed in ITER simulations with neon seeding with more complete model using kinetic neutrals and unbundled neon, has been used [26, 27]. In [27] the simulations have been group into different radiation levels, and  $c_{Ne,sep}$  is found to be  $\propto n_{e,sep}^{-2}$  at low radiated power, i.e. low  $c_{Ne,sep}$ , and  $\propto n_{e,sep}^{-4}$  at high radiated power. One can see in figure 2 that the DEMO modelling results of simulations within the operational space which have high impurity radiation agree with the  $c_{z,sep} \propto n_{e,sep}^{-4}$  scaling in ITER. As pointed out in [27], unfortunately there has been little attention to this in the experiments so far.

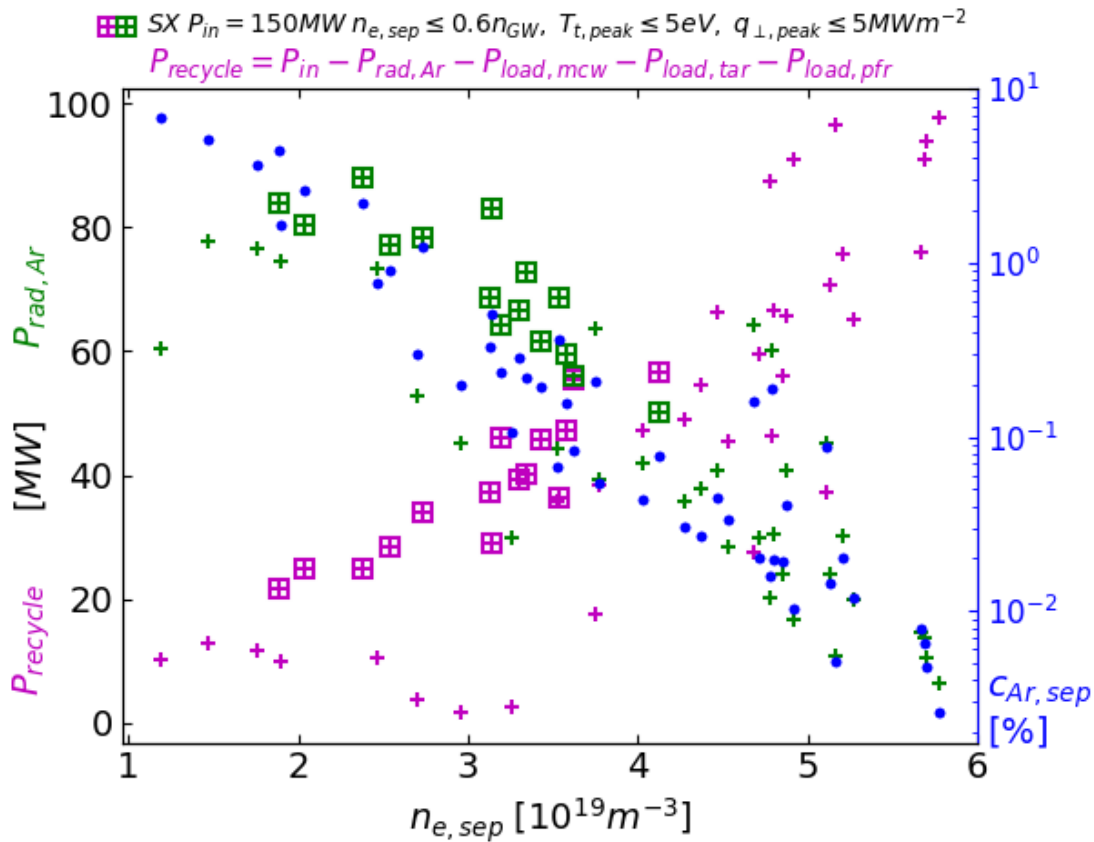


**Figure 8.** Radiated power by argon in the plasma,  $P_{rad,Ar}$  (green), the power available for ionizing deuterium neutrals,  $P_{recycle}$  (magenta), and the average argon concentration in the divertor region within the radial range of  $\lambda_q$  (blue), as a function of the OMP separatrix density, for DEMO SXD at  $P_{in}=150$  MW. The simulations within the operational space are marked with square symbols.

We next try to explain the drop of the main plasma density with Ar seeding in the simulations. The radiated power by argon is directly correlated with the increase of the concentration of this impurity, as shown in Figure 8. With Ar impurity radiating away more power from the plasma, from a power balance point of view, the power available for ionizing deuterium neutrals, coming from gas puff or from neutralization at PFC surfaces, is reduced. We define the parameter  $P_{recycle} = P_{in} - P_{rad,Ar} - P_{load,mcw} -$

$P_{load,pfr} - P_{load,tar}$  as a measure of the power available for getting deuterium neutrals ionized. Here  $P_{load,mcw}$ ,  $P_{load,pfr}$ ,  $P_{load,tar}$  are power deposited onto the main chamber wall, the plasma facing components below the private flux region (pfr), and the divertor targets. The  $P_{load,mcw}$ ,  $P_{load,pfr}$  term, resulted from radial transport, are relatively small and constant throughout the parameter scan in the SXD with  $P_{in}=150$  MW, standing at about 20% of the input power  $P_{in}$ . Figure 8 clearly reveals that there is evidently an *anti-correlation* between  $P_{rad,Ar}$  and  $P_{recycle}$  at fixed power input. As the former increases with the rising Ar concentration, the amount of power that goes into ionizing deuterium neutrals,  $P_{recycle}$ , drops from close to 100 MW at the highest to just about 20 MW at the lowest. Several data points of  $P_{recycle}$  (magenta '+' ) at intermediate densities of  $2 - 4 \times 10^{19} m^{-3}$  deviate from the linear trend. These are simulations in which the inner target and/or the outer target receive(s) high power load,  $P_{load,tar}$ , due to *not* sufficiently high upstream density or Ar radiation. Indeed, for the simulations within the operational space with  $T_t \leq 5$  eV, the anti-correlation between  $P_{rad,Ar}$  and  $P_{recycle}$  is much more clear.

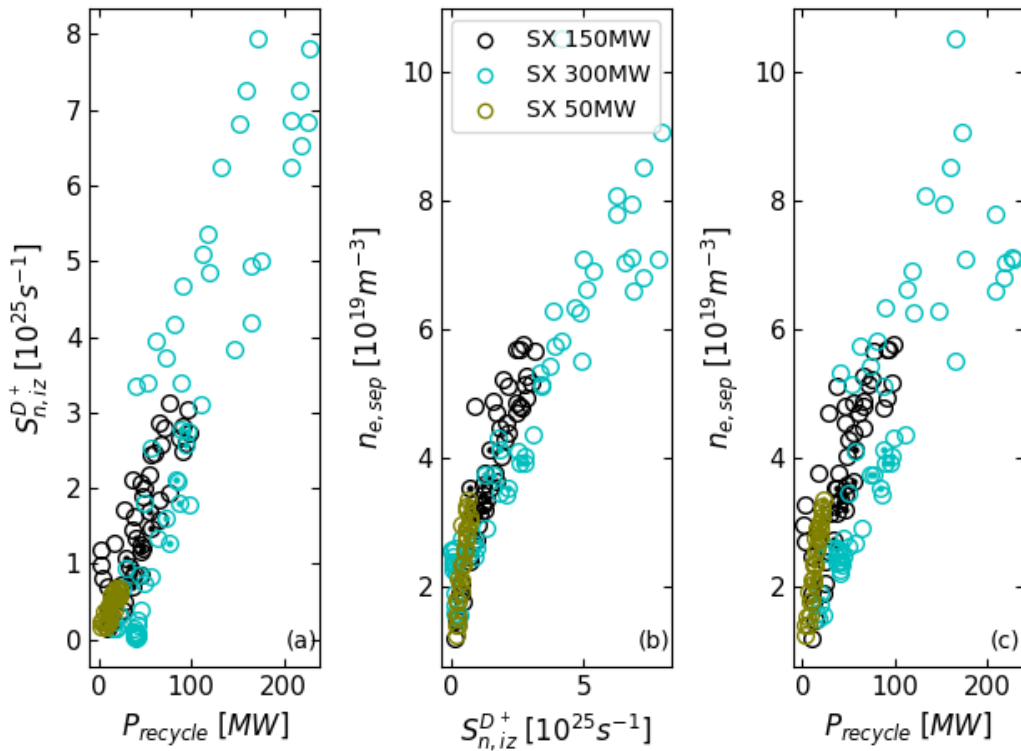


**Figure 9.** The correlation between  $P_{recycle}$  and  $S_n^{D+}$ ,  $S_n^{D+}$  and  $n_e$ ,  $P_{recycle}$  and  $n_e$  for the SXD simulations with low (50 MW), standard (150 MW) and high (300 MW) power input.  $P_{recycle}$  is the power available for ionizing the D neutrals, as defined in figure 8.  $S_n^{D+}$  is the ionization particle source of  $D^+$ .  $n_e$  is the density at OMP separatrix.

Ignoring the radiative loss during recombination of  $D^+$ , we have  $P_{recycle} = S_n^{D+} * (\epsilon_H^{pot} + \epsilon_H^{rad})$ , with  $\epsilon_H^{pot} = 13.6$  eV (no molecules in the simulation),  $\epsilon_H^{rad}$  being the mean

deuterium radiation loss per ionization event, and  $S_n^{D^+}$  being the particle source in  $[p/s]$ . As  $S_n^{D^+}$  concentrates in a narrow region of  $T_e = 5 - 10$  eV in the dense divertor plasma,  $\epsilon_H^{rad}$  does not vary much [28], yielding a linear dependence of  $S_n^{D^+}$  on  $P_{recycle}$ . This linear dependence between the two parameters is demonstrated in figure 9(a), for simulations of the DEMO SXD configuration at lower (50 MW), standard (150 MW) and higher (300 MW) input powers. The magnitude of the input power limits the range over which the power available for ionizing deuterium atoms can change. This then determines the range over which the ionization particle source can change in the simulations. The ionization particle source has a direct impact on the plasma density, as shown in figure 9(b). With more abundant ionization particle source in the plasma, the plasma density goes up. Finally, via the effect on the ionization particle source,  $P_{recycle}$  can affect the plasma density, as demonstrated in figure 9(c). The plasma density is positively correlated with the power that goes into ionizing the deuterium neutrals. Therefore the observation of plasma density dropping with increasing Ar concentration at each input power level is explained as the following: higher amount of Ar in the plasma enhances the radiated power which causes the power available for ionizing deuterium neutrals to decrease. This results in less ionization events of deuterium neutrals and consequently less particle (ions and electrons) source in the plasma. With less particle source available, the plasma density subsequently drops. The picture described here echoes the discussion in section 3.2.3 in [27].

## 5. Summary and Discussion

In this work, we have reported the following three key results found in the exploration of operational space in DEMO with super-X and conventional single-null divertors via fuelling, seeding and power level scans.

We find that the SXD configuration offers a larger margin to the limits on plasma density and impurity concentration of the operational space. Namely, at same upstream density (*argon concentration*) DEMO SXD has lower argon concentration (*upstream density*) at the vicinity of the confined plasma, compared to the DEMO SND. Utilizing the simple Lengyel model, we pin down the fundamental reason for the larger margin in SXD to be the longer parallel connection length from upstream to the outer target in this configuration. Furthermore, the SXD configuration features less radiation from above the X-point, and higher radiation from within the outer divertor, with respect to the SND configuration. In the divertor, the radiation is mainly confined close to the target in SXD at input power of 150 MW. On the contrast, in SXD with double the power (300 MW) and in SND (150 MW), the radiation in the divertor extends poloidally upwards to the X-point and spreads radially outward.

At input power of 300 MW, DEMO with the SX divertor still attains operational plasma states, whilst DEMO with the conventional SND does not. Comparing the 300 MW simulation to the standard 150 MW one at the same fuelling and seeding rates in the SXD configuration, both within the operational space, we find that the

radiated power by the argon impurity more than doubled, a more significant increase than that of the input power. The enhancement of the radiation is due to the elevated argon concentration in the divertor as well as the elevated upstream plasma density (*by* about 10%) and temperature (*by* about 40%), which result in higher electron pressure upstream and larger Lengyel integral in the divertor in the 300 MW simulations. This scheme can be well explained by the Lengyel model.

Finally we observe that the plasma density drops with increasing Ar concentration in DEMO in all configurations (SXD or conventional SND) and at all input power levels (50 MW, 150 MW, 300 MW). The most important reason for this is that argon impurity radiates away more power as the impurity concentration increases, leaving ever fewer power available for deuterium atoms to be ionized.

Even though simulations for current machines with kinetic neutrals, including molecules, the neutral-wall and neutral-neutral interactions, resulted in different neutral distributions and divertor plasma conditions than the simulations with fluid neutrals [19]. As already mentioned in section 1, the DEMO boundary plasma is dense enough that the neutrals' mean free path in the divertor is much smaller compared to the size of the divertor, justifying to some extent the treatment of neutrals as fluids in the simulations in this work. Nevertheless, the puffing and pumping in fluid neutrals model are treated in simplistic ways, posing concerns on the obtained results. However, We did pumping coefficient scan, and found that the plasma density is not sensitive to the scan in steady state. The  $c_z$  as a function of  $n_e$  based on Lengyel model is valid for plasma conditions at and after divertor detachment onset. In this work, we instead see that the simulations with one targets in attached condition (the *dots* with  $n_{e,sep} \leq 4.2 \times 10^{19} m^{-3}$  in the figure) also fit into the  $\bar{c}_{Ar,sep} - n_{e,sep}$  curve in figure 2. Further analysis is needed to understand why those simulations fit to the curve. Another detail is that, the  $c_z$  in the Lengyel model is the constant impurity concentration in the divertor region. In this work, we have chosen to focus on  $\bar{c}_{Ar,sep}$  as a measure of the impurity level in the immediate vicinity of the confined plasma out of interest of core dilution. We found that the Ar concentration in the outer divertor varies linearly with the Ar concentration along the separatrix, with the Ar enrichment, which is the ratio of Ar concentration in the divertor over that upstream, scattering only slightly between 1.0 to 3.0 in the simulations. Therefore  $\bar{c}_{Ar,sep}$  can be easily translated into  $\bar{c}_{Ar,div}$ . The activation of drifts, which is not done in the simulations in this study, may modify obtained divertor enrichment of argon as well as altering the in/out divertor asymmetry. We observe that the in/out divertor asymmetry is different between DEMO SXD and DEMO SND. In DEMO SND the outer divertor is always the hot one throughout the scans whereas the DEMO SXD has a more complicated picture. Either the inner or the outer divertor can be the hotter one, depending on the direction of a parallel thermo-electric current within the radial range of  $\lambda_{dq}$ . We will report these interesting results in another work in the near future.

Due to the use of fluid neutrals, bundled argon charge states and lack of drift effects in this study, the results reported here should be noted with some caution.

On the other hand, however, the simulations in this study have been carried out in a highly consistent way. We have set up simulations for all the configurations in identical ways and using same code. Therefore the comparative results reported here, e.g. the advantages observed in the SXD configuration for DEMO with respect to DEMO SND, should nevertheless be indicating.

## 6. REFERENCES

- [1] G. Federici, G. Giruzzi, C. Lowry, R. Kemp, D. Ward, R. Wenninger, and H. Zohm, “Eu demo design and r&d studies,” in *2013 IEEE 25th Symposium on Fusion Engineering (SOFE)*, pp. 1–8, June 2013.
- [2] W. Biel, R. Albanese, R. Ambrosino, M. Ariola, M. Berkel, I. Bolshakova, K. Brunner, R. Cavazzana, M. Ceconello, S. Conroy, A. Dinklage, I. Duran, R. Dux, T. Eade, S. Entler, G. Ericsson, E. Fable, D. Farina, L. Figini, C. Finotti, T. Franke, L. Giacomelli, L. Giannone, W. Gonzalez, A. Hjalmarsson, M. Hron, F. Janky, A. Kallenbach, J. Kogoj, R. König, O. Kudlacek, R. Luis, A. Malaquias, O. Marchuk, G. Marchiori, M. Mattei, F. Maviglia, G. De Masi, D. Mazon, H. Meister, K. Meyer, D. Micheletti, S. Nowak, C. Piron, A. Pironti, N. Rispoli, V. Rohde, G. Sergienko, S. El Shawish, M. Siccino, A. Silva, F. da Silva, C. Sozzi, M. Tardocchi, M. Tokar, W. Treutterer, and H. Zohm, “Diagnostics for plasma control – from iter to demo,” *Fusion Engineering and Design*, vol. 146, pp. 465 – 472, 2019. SI:SOFT-30.
- [3] G. Federici, C. Bachmann, L. Barucca, C. Baylard, W. Biel, L. Boccaccini, C. Bustreo, S. Ciattaglia, F. Cisondi, V. Corato, C. Day, E. Diegele, T. Franke, E. Gaio, C. Gliss, T. Haertl, A. Ibarra, J. Holden, G. Keech, R. Kembleton, A. Loving, F. Maviglia, J. Morris, B. Meszaros, I. Moscato, G. Pintsuk, M. Siccino, N. Taylor, M. Tran, C. Vorpahl, H. Walden, and J. You, “Overview of the DEMO staged design approach in europe,” *Nuclear Fusion*, vol. 59, p. 066013, apr 2019.
- [4] H. Lux, R. Kemp, D. Ward, and M. Sertoli, “Impurity radiation in demo systems modelling,” *Fusion Engineering and Design*, vol. 101, pp. 42 – 51, 2015.
- [5] H. Reimerdes, R. Ambrosino, P. Innocente, A. Castaldo, P. Chmielewski, G. D. Gironimo, S. Merriman, V. Pericoli-Ridolfini, L. Aho-Mantilla, R. Albanese, H. Bufferand, G. Calabro, G. Ciraolo, D. Coster, N. Fedorczak, S. Ha, R. Kembleton, K. Lackner, V. Loschiavo, T. Lunt, D. Marzullo, R. Maurizio, F. Militello, G. Ramogida, F. Subba, S. Varoutis, R. Zagórski, and H. Zohm, “Assessment of alternative divertor configurations as an exhaust solution for DEMO,” *Nuclear Fusion*, vol. 60, p. 066030, may 2020.
- [6] T. Hirai, F. Escourbiac, V. Barabash, A. Durocher, A. Fedosov, L. Ferrand, T. Jokinen, V. Komarov, M. Merola, S. Carpentier-Chouchana, N. Arkhipov, V. Kuznetsov, A. Volodin, S. Suzuki, K. Ezato, Y. Seki, B. Riccardi, M. Bednarek, and P. Gavila, “Status of technology r&d for the iter tungsten divertor monoblock,” *Journal of Nuclear Materials*, vol. 463, pp. 1248 – 1251, 2015. PLASMA-SURFACE INTERACTIONS 21.
- [7] J. You, E. Visca, C. Bachmann, T. Barrett, F. Crescenzi, M. Fursdon, H. Greuner, D. Guilhem, P. Languille, M. Li, S. McIntosh, A. Müller, J. Reiser, M. Richou, and M. Rieth, “European demo divertor target: Operational requirements and material-design interface,” *Nuclear Materials and Energy*, vol. 9, pp. 171 – 176, 2016.
- [8] M. Siccino, G. Federici, R. Kembleton, H. Lux, F. Maviglia, and J. Morris, “Figure of merit for divertor protection in the preliminary design of the EU-DEMO reactor,” *Nuclear Fusion*, vol. 59, p. 106026, aug 2019.
- [9] L. Aho-Mantila, F. Subba, D. Coster, L. Xiang, F. Militello, T. Lunt, D. Moulton, H. Reimerdes, M. Wensing, M. Wischmeier, R. Ambrosino, X. Bonnin, and M. Siccino, “Scoping the characteristics and benefits of a connected double-null configuration for power exhaust in eu-demo,” *Nuclear Materials and Energy*, vol. 26, p. 100886, 2021.

- [10] F. Militello, L. Aho-Mantila, R. Ambrosino, T. Body, H. Bufferand, G. Calabro, G. Ciraolo, D. Coster, G. D. Gironimo, P. Fanelli, N. Fedorczak, A. Herrmann, P. Innocente, R. Kembleton, J. Lilburne, T. Lunt, D. Marzullo, S. Merriman, D. Moulton, A. Nielsen, J. Omotani, G. Ramogida, H. Reimerdes, M. Reinhart, P. Ricci, F. Riva, A. Stegmeir, F. Subba, W. Suttrop, P. Tamain, M. Teschke, A. Thrysoe, W. Treutterer, S. Varoutis, M. Wensing, A. Wilde, M. Wischmeier, and L. Xiang, "Preliminary analysis of alternative divertors for demo," *Nuclear Materials and Energy*, p. 100908, 2021.
- [11] P. Stangeby, *The Plasma Boundary of Magnetic Fusion Devices*. IOP Publishing, 2000.
- [12] T. Petrie, J. Canik, C. Lasnier, A. Leonard, M. Mahdavi, J. Watkins, M. Fenstermacher, J. Ferron, R. Groebner, D. Hill, A. Hyatt, C. Holcomb, T. Luce, M. Makowski, R. Moyer, T. Osborne, and P. Stangeby, "Effect of changes in separatrix magnetic geometry on divertor behaviour in DIII-d," *Nuclear Fusion*, vol. 53, p. 113024, sep 2013.
- [13] X. BONNIN, W. DEKEYSER, R. PITTS, D. COSTER, S. VOSKOBOYNIKOV, and S. WIESEN, "Presentation of the new solps-iter code package fortokamak plasma edge modelling," *Plasma and Fusion Research*, vol. 11, no. 1403102, 2016.
- [14] S. Wiesen, D. Reiter, V. Kotov, M. Baelmans, W. Dekeyser, A. Kukushkin, S. Lisgo, R. Pitts, V. Rozhansky, G. Saibene, I. Veselova, and S. Voskoboynikov, "The new solps-iter code package," *Journal of Nuclear Materials*, vol. 463, pp. 480 – 484, 2015. PLASMA-SURFACE INTERACTIONS 21.
- [15] V. Rozhansky, E. Kaveeva, P. Molchanov, I. Veselova, S. Voskoboynikov, D. Coster, G. Counsell, A. Kirk, S. Lisgo, and and, "New b2solps5.2 transport code for h-mode regimes in tokamaks," *Nuclear Fusion*, vol. 49, p. 025007, jan 2009.
- [16] D. Reiter, "Eirene a monte carlo linear transport solver," 2002.
- [17] D. Reiter, M. Baelmans, and P. Börner, "The eirene and b2-eirene codes," *Fusion Science and Technology*, vol. 47, no. 2, pp. 172–186, 2005.
- [18] *ADAS416 Manual*.
- [19] X. Bonnin and D. Coster, "Full-tungsten plasma edge simulations with solps," *Journal of Nuclear Materials*, vol. 415, no. 1, Supplement, pp. S488 – S491, 2011. Proceedings of the 19th International Conference on Plasma-Surface Interactions in Controlled Fusion.
- [20] M. Bernert, M. Wischmeier, A. Huber, F. Reimold, B. Lipschultz, C. Lowry, S. Brezinsek, R. Dux, T. Eich, A. Kallenbach, A. Lebschy, C. Maggi, R. McDermott, T. Pütterich, and S. Wiesen, "Power exhaust by sol and pedestal radiation at asdex upgrade and jet," *Nuclear Materials and Energy*, vol. 12, pp. 111 – 118, 2017. Proceedings of the 22nd International Conference on Plasma Surface Interactions 2016, 22nd PSI.
- [21] A. Huber, M. Wischmeier, C. Lowry, S. Brezinsek, C. Maggi, M. Reinke, G. Sergienko, L. Aho-Mantila, G. Arnoux, M. Beurskens, M. Clever, S. Devaux, H. Esser, C. Giroud, M. Groth, S. Jachmich, A. Jarvinen, C. Linsmeier, B. Lipschultz, G. Matthews, G. Maddison, S. Marsen, P. A.G. Meigs, M. Nave, V. Philipps, M. Stamp, and S. Wiesen, "Impact of strong impurity seeding on the radiation losses in jet with iter-like wall," *41st EPS Conference on Plasma Physics*, 2014.
- [22] A. Loarte, J. W. Hughes, M. L. Reinke, J. L. Terry, B. LaBombard, D. Brunner, M. Greenwald, B. Lipschultz, Y. Ma, S. Wukitch, and S. Wolfe, "High confinement high radiated power h-mode experiments in alcator c-mod and consequences for iter," *Physics of Plasmas*, vol. 18, no. 5, p. 056105, 2011.
- [23] D. Eldon, E. Kolemen, D. Humphreys, A. Hyatt, A. Järvinen, A. Leonard, A. McLean, A. Moser, T. Petrie, and M. Walker, "Advances in radiated power control at diii-d," *Nuclear Materials and Energy*, vol. 18, pp. 285 – 290, 2019.
- [24] L. Lengyel, "Analysis of radiating plasma boundary layers," *IPP 1/191*, 1981.
- [25] M. Reinke, "Heat flux mitigation by impurity seeding in high-field tokamaks," *Nuclear Fusion*, vol. 57, p. 034004, jan 2017.
- [26] H. Pacher, A. Kukushkin, G. Pacher, V. Kotov, R. Pitts, and D. Reiter, "Impurity seeding in iter

- dt plasmas in a carbon-free environment,” *Journal of Nuclear Materials*, vol. 463, pp. 591 – 595, 2015. PLASMA-SURFACE INTERACTIONS 21.
- [27] R. Pitts, X. Bonnin, F. Escourbiac, H. Frerichs, J. Gunn, T. Hirai, A. Kukushkin, E. Kaveeva, M. Miller, D. Moulton, V. Rozhansky, I. Senichenkov, E. Sytova, O. Schmitz, P. Stangeby, G. De Temmerman, I. Veselova, and S. Wiesen, “Physics basis for the first iter tungsten divertor,” *Nuclear Materials and Energy*, vol. 20, p. 100696, 2019.
- [28] P. C. Stangeby, “Basic physical processes and reduced models for plasma detachment,” *Plasma Physics and Controlled Fusion*, vol. 60, p. 044022, mar 2018.